

Driven polymer translocation into a channel: Isoflux tension propagation theory and Langevin dynamics simulations

Jalal Sarabadani ^{1,*}, Ralf Metzler ² and Tapio Ala-Nissila^{3,4}

¹*School of Nano Science, Institute for Research in Fundamental Sciences (IPM), 19395-5531 Tehran, Iran*

²*Institute of Physics and Astronomy, University of Potsdam, 14476 Potsdam, Germany*

³*Department of Applied Physics and QTF Center of Excellence, Aalto University, P.O. Box 11000, 00076 Aalto, Espoo, Finland*

⁴*Interdisciplinary Centre for Mathematical Modelling and Department of Mathematical Sciences, Loughborough University, Loughborough, Leicestershire LE11 3TU, United Kingdom*



(Received 15 February 2022; accepted 10 May 2022; published 1 July 2022)

Isoflux tension propagation (IFTP) theory and Langevin dynamics (LD) simulations are employed to study the dynamics of channel-driven polymer translocation in which a polymer translocates into a narrow channel and the monomers in the channel experience a driving force f_c . In the high driving force limit, regardless of the channel width, IFTP theory predicts $\tau \propto f_c^\beta$ for the translocation time, where $\beta = -1$ is the force scaling exponent. Moreover, LD data show that for a very narrow channel fitting only a single file of monomers, the entropic force due to the subchain inside the channel does not play a significant role in the translocation dynamics and the force exponent $\beta = -1$ regardless of the force magnitude. As the channel width increases the number of possible spatial configurations of the subchain inside the channel becomes significant and the resulting entropic force causes the force exponent to drop below unity.

DOI: [10.1103/PhysRevResearch.4.033003](https://doi.org/10.1103/PhysRevResearch.4.033003)

I. INTRODUCTION

Starting with the seminal experimental works of Bezrukov *et al.* [1] and Kasianowicz *et al.* [2] as well as the theoretical study of Sung and Park [3], the understanding of the physical mechanisms behind the process of polymer translocation through a nanopore has attracted considerable interest from both experimental [4–12] and theoretical [3,13–56] groups. The process of polymer translocation has a wide variety of applications in many different areas, ranging from gene transfer between bacteria [57] and RNA transport through nuclear membrane pores [58], over DNA sequencing and drug delivery [59–61], to the filtration of polyelectrolytes by entropic ratchets [19].

The translocation of a polymer can be either driven [15,25,34] or unbiased [18,24,27,33]. There exist several scenarios for the driven case, e.g., the external driving force can be localized in the nanopore [25,34], can be due to interaction of chaperones [21,22] or active rods with the *trans* side subchain [56], or can be applied on the head monomer of the polymer (the end-pulled case [47]) by a magnetic or optical tweezers [7,9,12,62,63] or even by an atomic force microscope [64]. In the localized case in which the driving force acts on the monomer(s) inside the nanopore, the driving force

may alternate [26,65–67] and the process may be influenced by flickering of the nanopore [35,45]. The dynamics of the translocation process for all of the above scenarios has been theoretically described by the isoflux tension propagation (IFTP) theory [15,25,34,45,56]. In particular, in Ref. [45] the IFTP approach to pore-driven polymer translocation through a flickering nanopore under an alternating external driving force was studied for three different regimes of weak, moderate, and strong driving.

In the weakly driven or unbiased cases the entropic force, arising from the fact that the polymer chain can assume different configurations in space, plays an important role [3] and makes a significant contribution to the translocation dynamics. The spatial configurations of the chain can be controlled either by external fields and/or by the presence of a confining geometry [68,69]. An interesting realization occurs when the nanopore is replaced by a long nanochannel and the polymer is attracted into the channel by an external force acting on all monomers inside the channel (the “chain sucker”) [36]. As over time more monomers migrate into the channel, the net external driving force inside the channel naturally increases. In this case, due to the external channel driving force and the confinement by the channel, the *trans* side subchain possesses fewer spatial configurations with respect to the free space case. Consequently, the entropic force depends on both the channel driving force f_c and the channel diameter D , as we will demonstrate below.

For a polymer traversing a pore of finite length L , the total translocation time τ comprises three separate parts and can be written as $\tau = \tau_1 + \tau_2 + \tau_3$. Here τ_1 , τ_2 , and τ_3 correspond to pore filling, traversing through the pore, and pore emptying, respectively [70,71]. In the present work we focus on the case

*jalal@ipm.ir

Published by the American Physical Society under the terms of the [Creative Commons Attribution 4.0 International](https://creativecommons.org/licenses/by/4.0/) license. Further distribution of this work must maintain attribution to the author(s) and the published article's title, journal citation, and DOI.

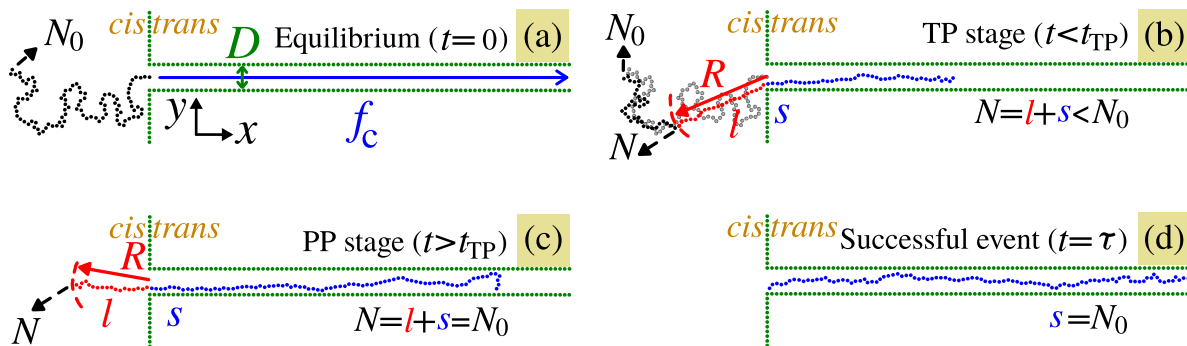


FIG. 1. (a) Chain configuration on the *cis* side after equilibration and before the filling process. The chain contour length and the channel width are $N_0 = 100$ and D , respectively. The external driving force f_c acts on the monomer(s) inside the channel (defined to be the *trans* side here) during the translocation process. (b) System configuration during the tension propagation (TP) stage when $t < t_{TP}$. Here R is the tension front location, s is the number of monomers on the *trans* side (translocation coordinate), l is the number of beads under the propagating tension on the *cis* side, and N is the number of all beads that are already influenced by the tension force. During the TP stage $N = l + s < N_0$, as the tension has not yet reached the chain end on the *cis* side. The chain part in gray is the polymer configuration at time zero, shown for comparison of the polymer configuration at time t with the one at time zero. (c) Same as (b) but for the postpropagation (PP) stage when $t > t_{TP}$. Here the whole chain including the last bead of the *cis* side chain end has already experienced the tension force and $N = l + s = N_0$. (d) Final configuration of the chain at the end of the translocation process.

where the pore length L is much longer than the polymer length N_0 , i.e., $L \gg N_0$, and thus the pore filling time τ_1 (see Fig. 1) is identified as the translocation time. Accordingly, the channel is considered to be the *trans* compartment in this process [36]. By using extensive Langevin dynamics (LD) simulations and the IFTP theory [25,34,42,45] we show that in the strong channel driving force limit and in the absence of the entropic force (or when the entropic force is much weaker than the driving) the scaling form for the filling time is given by $\tau \propto f_c^\beta$, where τ , f_c , and $\beta = -1$ are the average translocation time, the force acting on each individual monomer inside the channel, and the force scaling exponent, respectively. This dependence is the same as in the short-pore-driven translocation in the high force limit [15]. We also verify this result with LD simulations for a narrow channel that allows single-file translocation only. Further, we demonstrate that when the channel diameter D increases, the increased chain fluctuations inside the channel can cause deviations from the narrow-pore limit and the magnitude of the exponent β decreases.

With experimental setups similar to the scenario considered here, the genomic information has been visualized by studying DNA conformations inside long confining microchannels or nanochannels [72–76]. We expect that a comparison of such experiments with the observations reported here may lead to a further quantitative testing of the predictions of translocation theory.

The outline of the paper is as follows. We present details of the simulation methods in Sec. II and introduce the IFTP approach in Sec. III. Section IV is devoted to the results, comparing IFTP predictions with the behavior observed in the LD simulations. A summary and conclusions are given in Sec. V.

II. LANGEVIN DYNAMICS SIMULATIONS

For numerical accuracy and efficiency we consider here a two-dimensional system which is well justified for confined systems in particular. We note that the theory contains the

general Flory scaling exponent that has different values in two and three dimensions. The two-dimensional system under consideration is composed of a linear, flexible self-avoiding polymer modeled by a bead-spring model [77] and a rigid membrane including a long channel as depicted in Fig. 1. The interaction between any two bonded monomers is the sum of the Weeks-Chandler-Anderson (WCA) and finitely extensible nonlinear elastic (FENE) potentials. The WCA potential is the repulsive

$$U_{\text{WCA}}(r) = \begin{cases} U_{\text{LJ}}(r) - U_{\text{LJ}}(r_c) & \text{if } r \leq r_c \\ 0 & \text{if } r > r_c, \end{cases} \quad (1)$$

where $r_c = 2^{1/6}$ is the cutoff radius and $U_{\text{LJ}}(r)$ is the Lennard-Jones (LJ) potential

$$U_{\text{LJ}}(r) = 4\epsilon \left[\left(\frac{\sigma}{r} \right)^{12} - \left(\frac{\sigma}{r} \right)^6 \right], \quad (2)$$

where ϵ is the depth of the potential well, σ is the radius of each monomer, and r is the monomer-monomer distance. Nearest-neighbor monomers interact via the FENE potential

$$U_{\text{FENE}}(r) = -\frac{1}{2}kR_0^2 \ln \left(1 - \frac{r^2}{R_0^2} \right), \quad (3)$$

where R_0 and k are the maximum distance allowed between the neighboring monomers and the effective spring constant, respectively. All nonbonded interactions are given by the WCA potential. The contour length of the polymer in LJ units is $N_0 = 100$ and the channel length $L = 200$ is larger than N_0 .

The simulation box dimensions are $L_x = 400$ and $L_y = 300$ in the x and y directions, respectively, with periodic boundaries in the y direction. The membrane walls inside and outside the pore are made of spatially fixed (frozen) particles located at distance σ from each other (green dots in Fig. 1). The interactions between monomers and frozen particles (membrane and nanochannel particles) are governed by the repulsive WCA potential. In Fig. 1(a) D denotes the channel width that varies as $D = 2, 3, 4.5$, and 6 in the LD simulations. The external driving force f_c [depicted in Fig. 1(a) in

blue], acts horizontally on each individual monomer inside the channel and assumes the values $f_c = 0.2, 0.3, 0.5,$ and 1.2 (in LJ units). The resulting dynamical equation for the position vector \mathbf{r}_i of monomer i then reads

$$M\dot{\mathbf{r}}_i = -\eta\dot{\mathbf{r}}_i - (\nabla U_i) + \xi_i(t), \quad (4)$$

where M is the monomer mass, η is the solvent friction coefficient, and U_i is the sum of all interactions of the i th monomer. Here ξ_i represents a thermal white noise vector with zero mean $\langle \xi_i(t) \rangle = \mathbf{0}$ and correlation $\langle \xi_i(t) \cdot \xi_j(t') \rangle = 4\eta k_B T \delta_{ij} \delta(t - t')$, where k_B and T are the Boltzmann constant and temperature, respectively, δ_{ij} is the Kronecker, and $\delta(t - t')$ is the Dirac delta function. Moreover, $\sigma, M,$ and ε are used as the units of length, mass, and energy, respectively. The diameter of the monomers is $\sigma = 1$, and this also determines the size of each channel or membrane particle. The mass of each monomer and other particles in the system is given by $M = 1$. We choose $\varepsilon = 1$, $\eta = 0.7$, and $k_B T = 1.2$. The time unit for the simulations is defined as $\tau_0 = \sqrt{M\sigma^2/\varepsilon}$. The maximum allowed distance between two bonded monomers is $R_0 = 1.5$, and $k = 30$ is the spring constant.

All LD simulations were performed by using the LAMMPS [78] package. In our model the size of each bead is about 1.5 nm in real units, which corresponds approximately to the Kuhn length of single-stranded DNA, the mass of each bead is about 936 amu, and the strength of interaction is 3.39×10^{-21} J at $T = 295$ K (room temperature). Therefore, the force and timescales in LJ units are approximately 2.3 pN and 32.1 ps, respectively.

Within IFTP theory below we use dimensionless quantities, denoted by the tilde, as $\tilde{Y} \equiv Y/Y_u$. Here the denominator indicates the units of time, length, monomer flux, velocity, force, and friction as $t_u \equiv \eta\sigma^2/(k_B T)$, $s_u \equiv \sigma$, $\phi_u \equiv k_B T/(\eta\sigma^2)$, $v_u \equiv \sigma/t_u = k_B T/(\eta\sigma)$, $f_u \equiv k_B T/\sigma$, and $\Gamma_u \equiv \eta$, respectively. The parameters without the tilde symbol are expressed in LJ units.

Before the actual translocation process, the head monomer of the polymer chain is fixed in the center of the entrance of the channel (pore) and the polymer is equilibrated. Then the fixed head monomer is released and at the same time the external channel driving force f_c is switched on. To obtain sufficient statistics, averaging is performed over 1000 uncorrelated trajectories. Figure 1(a) shows a typical equilibrium state of the polymer chain (from LD simulations) just before starting the translocation process. Figures 1(b) and 1(c) correspond to the tension propagation (TP) and post propagation (PP) stages, respectively. Finally, Fig. 1(d) presents the configuration of the chain inside the channel just at the termination of translocation process, which equals the filling time $\tau_1 = \tau$ here. In the TP stage presented in Fig. 1(b) $t < t_{TP}$, as the chain translocates into the channel by the external channel driving force f_c acting on each individual monomer inside the nanopore, tension propagates along the backbone of the subchain on the *cis* side. The snapshot, at time t , in Fig. 1(b) shows that s monomers (in blue) have translocated into the channel, while l monomers (in red) on the *cis* side have been influenced by the tension force and are moving towards the channel, i.e., $N = s + l$ is the number of all monomers that have been influenced by the tension force up to time t . The

remaining $N_0 - N$ monomers are at equilibrium and have zero net velocity (monomers in black). In the TP stage, as the tension force has not reached the chain end, we thus have $N = s + l < N_0$.

The picture above shows that the subchain on the *cis* side can be divided into two parts, a mobile part (in red) and an equilibrium part (in black). The location of the tension front, that is, the border between the mobile and equilibrium parts, is specified by R . The gray monomers represent the configuration of the polymer at time zero, for comparison of the polymer configurations at times t and zero. The snapshot of the system (from LD simulation) is shown in Fig. 1(c) for $t > t_{TP}$. At time t_{TP} , the tension propagation time, the tension reaches the chain end on the *cis* side, and by that time all monomers of the chain have already been influenced by the tension force, i.e., $N = l + s = N_0$. Finally, Fig. 1(d) illustrates the configuration of the chain just at the termination of the translocation process, when the entire polymer chain has been translocated inside the *trans* side nanochannel.

III. ISOFLUX TENSION PROPAGATION THEORY

The quantitatively accurate IFTP theory can be employed to describe the dynamics of the translocation process for the channel-driven case. To this end we generalize the IFTP theory by considering the effective force acting on the monomer(s) located just at the entrance of the channel. The dynamics of the translocation process can be unraveled by solving the equation of motion for the time evolution of the translocation coordinate \tilde{s} within the isoflux (IF) approximation for the monomer flux $\tilde{\phi} = d\tilde{s}/d\tilde{t}$. In the IF approximation the monomer flux in the mobile part of chain [*cis* side, red monomers in Figs. 1(b) and 1(c)] is spatially constant but evolves in time.

To obtain the equation of motion for \tilde{s} , the tension force $\tilde{\mathbb{F}}(\tilde{x}, \tilde{t})$ at the distance \tilde{x} from the channel entrance on the *cis* side is needed. Integrating the local force-balance equation $d\tilde{\mathbb{F}}(\tilde{x}', \tilde{t}) = -\tilde{\phi}(\tilde{t})d\tilde{x}'$ over the distance from the channel entrance at $\tilde{x}' = 0$ to the distance $\tilde{x}' = \tilde{x}$ from the channel entrance, the tension force at distance \tilde{x} on the *cis* side is written as $\tilde{\mathbb{F}}(\tilde{x}, \tilde{t}) = \tilde{\mathbb{F}}_0 - \tilde{x}\tilde{\phi}(\tilde{t})$, where $\tilde{\mathbb{F}}_0 = \tilde{f}(\tilde{t}) - \tilde{\eta}_c\tilde{\phi}(\tilde{t})$ is the tension force just at the entrance of channel on the *cis* side in terms of the channel friction coefficient $\tilde{\eta}_c$ and the effective force $\tilde{f}(\tilde{t})$ acting on the monomer(s) just inside the entrance of the channel (see the discussion below and the schematic in Fig. 2). Using the fact that the tension force vanishes at the tension front, i.e., $\tilde{\mathbb{F}}(\tilde{x} = \tilde{R}, \tilde{t}) = 0$, the tension force just at the entrance of channel is related to \tilde{R} via $\tilde{\mathbb{F}}_0 = \tilde{R}(\tilde{t})\tilde{\phi}(\tilde{t})$. Combining this with the definition of the monomer flux, the equation of motion for the translocation coordinates \tilde{s} is obtained as

$$[\tilde{R}(\tilde{t}) + \tilde{\eta}_c] \frac{d\tilde{s}}{d\tilde{t}} = \tilde{f}(\tilde{t}). \quad (5)$$

The expression in square brackets is the effective friction and is the sum of friction due to the *cis* side mobile subchain $\tilde{R}(\tilde{t})$ and the channel friction $\tilde{\eta}_c$. To solve the above equation, the time evolution of $\tilde{f}(\tilde{t})$ and $\tilde{R}(\tilde{t})$ must be known. We first explain how $\tilde{f}(\tilde{t})$ can be obtained numerically and then the

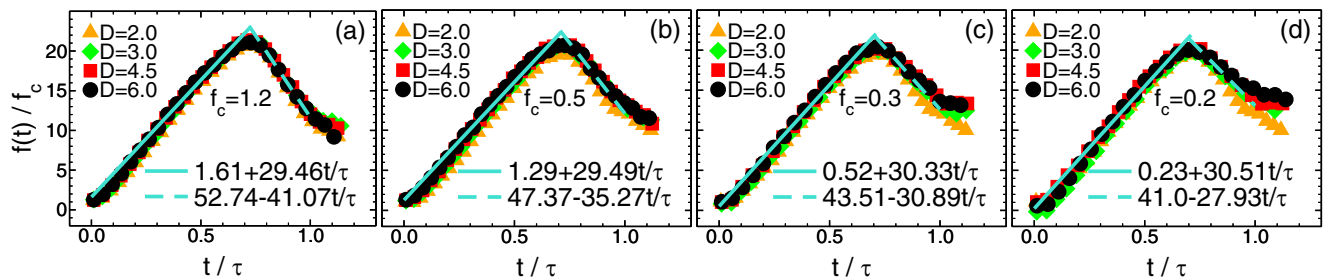


FIG. 2. (a) Normalized effective force $f(t)/f_c$ as a function of normalized time t/τ , for fixed channel driving force $f_c = 1.2$, evaluated for the channel widths $D = 2.0$ (orange triangles), 3.0 (green diamonds), 4.5 (red squares), and 6.0 (black circles). Turquoise solid and dashed lines are fitting curves to the normalized forces in the TP and PP stages, respectively (see the text). (b)–(d) Same as (a) but for $f_c = 0.5, 0.3$, and 0.2 , respectively.

equation of motion for the time evolution of $\tilde{R}(\tilde{t})$ can be extracted within the IF approximation.

We performed extensive LD simulations to obtain the effective driving force $f(t)$, which is the force experienced by the monomer inside the channel entrance (i.e., the x component of its position is in the region $-0.5 < x < 0.5$). The channel driving force f_c , the force f_{LJ} due to the other monomers inside the channel in the region of $x > 0.5$, and the interaction between the channel wall particles and the monomer(s) inside the entrance of the channel contribute to the total effective driving force $f(t)$. The contribution of f_{LJ} to the driving is the combination of the FENE-bond force and nonbonded repulsive LJ interactions (WCA).

Figure 2(a) presents the normalized effective driving force $f(t)/f_c$ as a function of the normalized time t/τ , where τ is the translocation time, for constant channel driving force $f_c = 1.2$ and for the channel diameters $D = 2, 3, 4.5$, and 6 . For each set of parameters the effective driving force is obtained by averaging over 1000 uncorrelated trajectories. Figures 2(b)–2(d) are the same as Fig. 2(a) but for the channel driving forces $f_c = 0.5, 0.3$, and 0.2 , respectively. We can see from Fig. 2 that data for fixed f_c collapse on a master curve. The effective force $f(t)$ first linearly grows and reaches its maximum and then decreases. The maximum occurs at the tension propagation time t_{TP} for all curves. This has been checked by considering the bond length distributions in Appendix A (see Fig. 9) and also by looking at the average velocity distributions of monomers in Appendix B (see Fig. 10) at different instants during the translocation process. Both bonds and velocity distributions confirm that for all sets of parameters the PP stage starts around time $t_{TP} \approx 0.7\tau$. As Fig. 2 shows, in the TP and PP stages the driving force can be written as

$$\begin{aligned} \frac{\tilde{f}_{TP}(\tilde{t})}{f_c} &= a + \frac{b\tilde{t}}{\tilde{\tau}}, \\ \frac{\tilde{f}_{PP}(\tilde{t})}{f_c} &= c - \frac{d\tilde{t}}{\tilde{\tau}}, \end{aligned} \quad (6)$$

respectively. For strong channel driving force $f_c = 1.2$ in Fig. 2(a), the values of the constants are $a = 1.61$, $b = 29.46$, $c = 52.74$, and $d = 41.07$, and for weaker channel driving forces the values of a , b , c , and d can be found in the corresponding panels. At the tension propagation time t_{TP} , the values of the effective forces in the TP and PP stages should be

equal (continuity condition), i.e., $\tilde{f}_{TP}(\tilde{t} = t_{TP}) = \tilde{f}_{PP}(\tilde{t} = t_{TP})$. Consequently, $\tilde{t}_{TP} = Q\tilde{\tau}$, where $Q = (c - a)/(b + d)$, with the approximate value of 0.7 .

Based on the time evolution of the total effective driving force $\tilde{f}(\tilde{t})$, one can solve the effective force-balance equation (5), provided the time evolution of the tension front location $\tilde{R}(\tilde{t})$ is known. The equation of motion for $\tilde{R}(\tilde{t})$ in the TP stage is obtained by comparing the average spatial configurations of the chain at time zero [typical chain configuration in gray at time zero in Fig. 1(b)] and at time \tilde{t} [typical chain configuration in blue, red, and black in Fig. 1(b)]. The number of those monomers that at equilibrium (at time zero) are located between the entrance of the channel and the tension front (at time \tilde{t}) is, on average, the same as the number of monomers influenced by the tension force by the time \tilde{t} , i.e., $N = \tilde{s} + \tilde{l}$, the sum of the monomers in blue inside the channel and the mobile monomers in red on the *cis* side at time \tilde{t} . Then in equilibrium the size of the subchain that occupies the region between the entrance of the channel and the tension front is \tilde{R} . Therefore, according to Flory theory, one can write the end-to-end distance devoted to this portion of the polymer chain as $\tilde{R} = A_\nu N^\nu$. Combining this end-to-end distance with the fact that $N = \tilde{s} + \tilde{l}$ and taking the time derivative of both sides of $\tilde{R} = A_\nu(\tilde{s} + \tilde{l})^\nu$ in the strong stretching (SS) regime where the mobile subchain on the *cis* side is fully straightened ($\tilde{l} = \tilde{R}$), the equation of motion for the tension front location in the TP stage is obtained as

$$\dot{\tilde{R}}(\tilde{t}) = \frac{\nu A_\nu^{1/\nu} \tilde{R}(\tilde{t})^{(\nu-1)/\nu} \tilde{\phi}(\tilde{t})}{1 - \nu A_\nu^{1/\nu} \tilde{R}(\tilde{t})^{(\nu-1)/\nu}}, \quad (7)$$

where the definition $\tilde{\phi} = d\tilde{s}/d\tilde{t}$ of the monomer flux has been used. Conversely, in the PP stage, in which the tension has reached the chain end on the *cis* side, the closure relation is $N = \tilde{s} + \tilde{l} = N_0$. Performing the time derivative on both sides of this closure relation in the SS regime, in which $\tilde{l} = \tilde{R}$, yields the equation of motion for the tension front,

$$\dot{\tilde{R}}(\tilde{t}) = -\tilde{\phi}(\tilde{t}). \quad (8)$$

To have a full solution, in the TP stage equations (5) and (7) need to be solved self-consistently, while the PP stage is based on Eqs. (5) and (8).

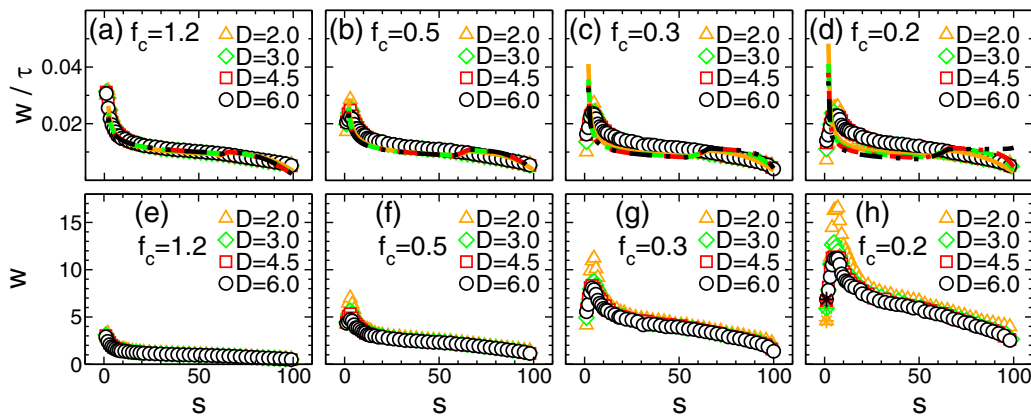


FIG. 3. (a) Normalized waiting time w/τ as a function of the translocation coordinate s , for fixed value $f_c = 1.2$ of the channel driving force and the channel widths $D = 2.0$ (orange triangles), 3.0 (green diamonds), 4.5 (red squares), and 6.0 (black circles). Orange solid, green dashed, red dash-dotted, and black dash-double-dotted lines represent the IFTP results in the strong stretching regime for channel widths $D = 2.0, 3.0, 4.5,$ and 6.0 , respectively (not shown in the legend). (b)–(d) Same as (a) but for $f_c = 0.5, 0.3,$ and 0.2 , respectively. (e)–(h) Same as (a)–(d), respectively, but for the unnormalized waiting time distribution w as a function of s . The values of the channel friction coefficients in the IFTP theory have been chosen as $\eta_c = 4.3, 3.0, 2.5,$ and 2.3 , corresponding to different channel widths $D = 2, 3, 4.5,$ and 6 , respectively [39].

IV. RESULTS

This section is devoted to the presentation of the results from the IFTP theory and LD simulations for the translocation dynamics at both the monomer and global levels. To this end, the waiting time distribution, translocation time, monomer mean-square displacement, and the monomer density are investigated.

A. Waiting time distribution

One of the most important quantities that reveals the dynamics of the translocation process at the monomer level is the distribution w of waiting times (WTs), the time that each bead spends at the entrance of the nanochannel (specifically when the x component of the position vector of the corresponding bead is in the region $-0.5 \leq x \leq +0.5$) during the translocation process. Figure 3(a) shows the normalized WT distribution w/τ as a function of the translocation coordinate s , for fixed value $f_c = 1.2$ of the driving force and the channel widths $D = 2.0$ (orange triangles), 3.0 (green diamonds), 4.5 (red squares), and 6.0 (black circles). Orange solid, green dashed, red dash-dotted, and black dash-double-dotted lines represent the IFTP results in the SS regime for channel widths $D = 2.0, 3.0, 4.5,$ and 6.0 , respectively (not shown in the legend). Figures 3(b)–3(d) are the same as Fig. 3(a) but for $f_c = 0.5, 0.3,$ and 0.2 , respectively. The values of the channel friction coefficients that have been used in the IFTP theory are $\eta_c = 4.3, 3.0, 2.5,$ and 2.3 , corresponding to different channel widths $D = 2, 3, 4.5,$ and 6 , respectively [39].

We can conclude from the data that the results of the IFTP theory increasingly deviate from the LD data as the value of the driving force decreases. This happens due to the fact that here we only consider the SS regime (the mobile subchain in the *cis* side is fully straightened) in IFTP theory in the absence of the entropic force. This discrepancy can be resolved in the weak and intermediate force regimes by taking the entropic force into account. There the spatial shape of the

mobile subchain on the *cis* side assumes the so-called trumpet and stem-flower shapes [34,42], respectively. However, this is beyond the scope of the present study. However, the global dynamics of the translocation process is well explained by the IFTP theory in the high force limit (here $f_c = 1.2$) by the SS regime.

In Figs. 3(e)–3(h), which correspond to Figs. 3(a)–3(d), respectively, the unnormalized WT distribution w is shown as a function of s . As seen in Fig. 3(e), regardless of the channel width, for the highest value $f_c = 1.2$ of the driving force the WT monotonically decreases as s increases. For smaller values of the driving force $f_c \leq 0.5$ the WT curve is no longer monotonic and a hump appears for small s . This effect is more pronounced either by decreasing the value of the driving force, from Fig. 3(f) to Fig. 3(h), or at constant driving force, i.e., in each of Figs. 3(f)–3(h), by decreasing the channel width from $D = 6$ to $D = 2$.

The reason for the monotonicity of the WT curve in Fig. 3(e) is that for strong driving with $f_c = 1.2$, at the beginning of the translocation process the tension propagates very fast and the subchain in the vicinity of the channel entrance resists the driving force. This leads to the large value of the WT at the beginning of the process. At later moments, when more monomers traverse the channel entrance, the total net force acting on the *trans* side subchain increases and the value of the WT decreases. Therefore, for strong driving the WT monotonically decreases. On the other hand, for weaker driving force in Figs. 3(f)–3(h), at the very beginning of the translocation process, the entropic force due to spatial fluctuations of the *cis* side chain configurations that resists translocation is more pronounced for the wide channels, leading to the larger WT for the channel with $D = 6$ and smaller values for $D = 2$ [asterisks in Fig. 3(h)]. Then with time more monomers experience the friction due to the mobile part of the *cis* side subchain, while the driving is not strong and s does not increase fast enough. Consequently, the WT increases at the starting moments of the translocation process. At the later time, as enough monomers have already traversed the channel

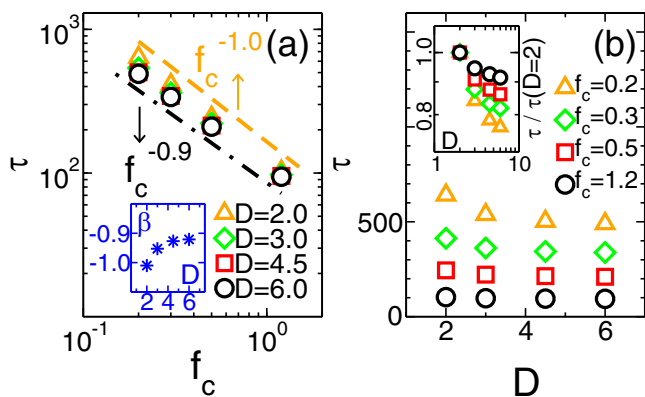


FIG. 4. (a) Translocation time τ as a function of the channel driving force f_c , for channel widths $D = 2.0$ (orange triangles), 3.0 (green diamonds), 4.5 (red squares), and 6.0 (black circles). The orange dashed and black dash-dotted lines are fits to the data with $D = 2.0$ and 6.0 , respectively, but shifted for better visibility. The inset shows the force exponent β of the scaling form $\tau \propto f_c^\beta$ as a function of the channel width D . (b) Translocation time τ as a function of D , for $f_c = 0.2$ (orange triangles), 0.3 (green diamonds), 0.5 (red squares), and 1.2 (black circles). The inset shows the normalized translocation time $\tau/\tau(D = 2)$ as a function of D .

entrance, the net effective driving force becomes large enough to accelerate the translocation process and therefore the WT decreases. At constant driving force, the nonmonotonicity in the WT curves is more pronounced with decreasing channel width. This is due to the fact that decreasing channel width increases the effective channel friction making the translocation dynamics slower and thus the hump in the WT curve is more pronounced.

B. Scaling of translocation time

The fundamental quantity that reveals the global dynamics of the translocation process is the translocation time τ , which is the average time for the whole chain to enter the channel and fully translocate to the *trans* side channel of the system. In Fig. 4 we show the translocation times τ from LD simulations. In Fig. 4(a) τ is shown as a function of the driving force f_c for the channel diameters $D = 2$ (orange triangles), 3 (green diamonds), 4.5 (red squares), and 6 (black circles). The orange dashed and black dash-dotted lines are fits to the data with $D = 2$ and 6 , respectively, but shifted for better visibility. The inset shows the force exponent β from the scaling relation $\tau \propto f_c^\beta$ as a function of D . The exponent β approaches -1 as the channel width decreases to 2 . In Fig. 4(b) τ is shown as a function of D for $f_c = 0.2$ (orange triangles), 0.3 (green diamonds), 0.5 (red squares), and 1.2 (black circles). In the strong force limit, i.e., for $f_c = 1.2$, τ does not change appreciably (black circles), while for the weakest force $f_c = 0.2$ the translocation time increases as the channel width decreases (orange triangles). This is confirmed in the inset of Fig. 4(b), where the normalized translocation time $\tau/\tau(D = 2)$ is shown as a function of D on a log-log scale. The symbols in the inset are the same as those of the main Fig. 4(b).

The scaling form for the translocation time can be analytically obtained from IFTP theory in the SS limit. To this end

one needs to integrate N in the TP stage from 0 to N_0 , and in the PP stage \tilde{R} should be integrated from $R(N_0)$ to 0 . These integrals are performed by combining the mass conservation in the TP stage, $N = \tilde{s} + \tilde{l}$, and in the PP stage, $N = \tilde{s} + \tilde{l} = N_0$, with Eq. (5) [42]. Then, summing up the TP and PP times, the relation for $\tilde{\tau}$ is given in the form [56]

$$\int_0^{\tilde{\tau}_{\text{TP}}} \tilde{f}_{\text{TP}}(\tilde{t}) d\tilde{t} + \int_{\tilde{\tau}_{\text{TP}}}^{\tilde{\tau}} \tilde{f}_{\text{PP}}(\tilde{t}) d\tilde{t} = \int_0^{N_0} dN [\tilde{R}(N) + \tilde{\eta}_c], \quad (9)$$

where $\tilde{f}_{\text{TP}}(\tilde{t})$ and $\tilde{f}_{\text{PP}}(\tilde{t})$ are determined by Eq. (6). Combining Eqs. (9) and (6) and using the closure relation $\tilde{R} = A_\nu N^\nu$, where $A_\nu = 1.1$ (from LD data) for the end-to-end distance in the TP stage and $\nu = 3/4$ is the Flory exponent in two dimensions, the translocation time is given by [56]

$$\tilde{\tau} = \left[\frac{A_\nu N_0^{1+\nu}}{1+\nu} + N_0 \tilde{\eta}_c \right] / (G \tilde{f}_c), \quad (10)$$

where $G = -0.5(c - a)^2/(b + d) + c - d/2 \approx 13.7$ for Fig. 2(a). Equation (10) shows that the translocation time scales with the channel driving force as $\tilde{\tau} \propto \tilde{f}_c^{-1}$, i.e., for the SS regime the force exponent is $\beta = -1$. Moreover, the effective translocation exponent α that is defined via $\tilde{\tau} \propto N_0^\alpha$ is bounded between 1 and $1 + \nu$, i.e., $1 < \alpha < 1 + \nu$, due to the competition between the two terms in square brackets in Eq. (10), in which the first and second terms originate from the *cis* side and channel frictions, respectively. The lower and upper bounds are assumed in the very short and very long chain limits, respectively [42].

To compare the scaling result of Eq. (10) with the LD simulation data, the inset of Fig. 4(a) shows the force exponent β from LD as a function of the channel width D . As the channel width decreases β moves closer to -1 . The reason for this is that as an increasing channel diameter allows more pronounced spatial fluctuations of the *trans* side subchain, leading to an increased entropic force. Consequently, the force exponent β changes as a function of the channel diameter. For the minimum channel width $D = 2$ the force exponent assumes its ideal value $\beta = -1$, due to negligible configurational fluctuations of the subchain on the *trans* side [see Fig. 4(a)]. This is the value in Eq. (10) from IFTP theory. Moreover, as shown in the inset of Fig. 4(a), increasing the channel width changes the value of the force exponent toward its asymptotic value $\beta \sim -0.9$ for a very wide channel, corresponding to a half space with infinite D [39]. It should be mentioned that at high channel driving forces the force exponent approaches $\beta = -1$ regardless of the channel width, as in this limit the value of the driving force by far exceeds the entropic one.

To investigate the effect of the entropic force on the translocation time, the inset of Fig. 4(b) shows the normalized translocation time $\tau/\tau(D = 2)$ as a function D for various values of f_c . As can be seen, the deviation of τ from the value for $D = 2$ (when the entropic force is negligible due to the small configurational fluctuations of the *trans* side subchain) grows with increasing D . This is more pronounced at weaker driving forces, again due to the fact that by increasing D the entropic force plays a more important role.

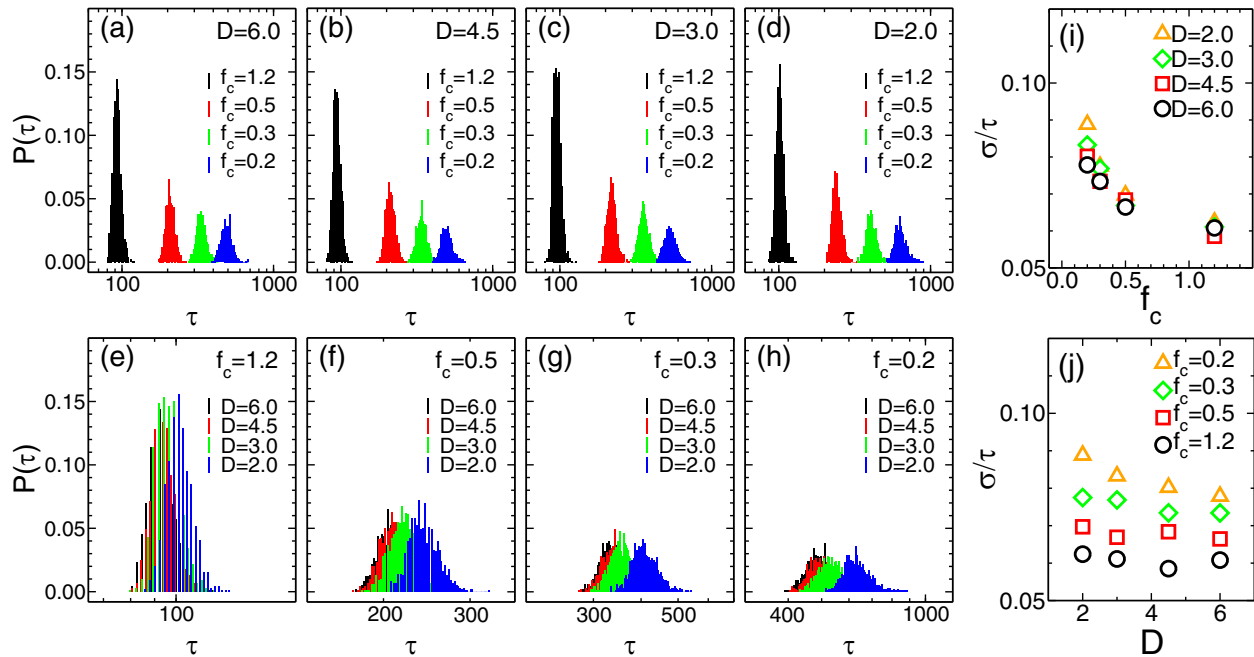


FIG. 5. (a) Probability distribution $P(\tau)$ of translocation times as a function of translocation time τ , for fixed channel width $D = 6.0$ and channel driving force $f_c = 1.2$ (black bars), 0.5 (red bars), 0.3 (green bars), and 0.2 (blue bars). (b)–(d) Same as (a) but for $D = 4.5$, 3.0, and 2.0, respectively. (e) Probability distribution $P(\tau)$ as a function of τ , for fixed $f_c = 1.2$ and $D = 6.0$ (black bars), 4.5 (red bars), 3.0 (green bars), and 2.0 (blue bars). (f)–(h) Same as (e) but for $f_c = 0.5$, 0.3, and 0.2, respectively. All panels are in log-linear scale. (i) Normalized standard deviation σ/τ as a function of f_c for $D = 2.0$ (orange triangles), 3.0 (green diamonds), 4.5 (red squares), and 6.0 (black circles). (j) Normalized standard deviation σ/τ as a function of D for $f_c = 2.0$ (orange triangles), 0.3 (green diamonds), 0.5 (red squares), and 1.2 (black circles).

C. Distribution of translocation times

We next study the effect of the channel driving force f_c as well as the channel diameter D on the distribution $P(\tau)$ of translocation times τ . Figure 5(a) shows $P(\tau)$ as a function of τ for fixed contour length $N_0 = 100$ and channel width $D = 6$, for the channel driving force values $f_c = 1.2$ (black bars), 0.5 (red bars), 0.3 (green bars), and 0.2 (blue bars). Figures 5(b)–5(d) are the same as Fig. 5(a) but for channel widths $D = 4.5$, 3, and 2, respectively. As can be seen in each panel, decreasing channel driving force increases the mean translocation time, and $P(\tau)$ becomes wider (note the logarithmic scale on the horizontal axis). This is again due to the fact that decreasing f_c allows more substantial spatial fluctuations of the mobile subchain on the *cis* and *trans* sides. Consequently, the fluctuations of translocation times increase as well. In Fig. 5(e) $P(\tau)$ is shown as a function of τ for a fixed value of $f_c = 1.2$ and for channel widths $D = 6.0$ (black bars), 4.5 (red bars), 3.0 (green bars), and 2.0 (blue bars). Figures 5(f)–5(h) are the same as Fig. 5(e) but for channel driving forces $f_c = 0.5$, 0.3, and 0.2, respectively. As can be seen from Figs. 5(e)–5(h) decreasing f_c leads to increasing separation of the distributions in each panel.

To quantify the distinctions, in Fig. 5(i) the normalized standard deviation σ/τ is shown as a function of f_c for the channel widths $D = 2.0$ (orange triangles), 3.0 (green diamonds), 4.5 (red squares), and 6.0 (black circles). Moreover, Fig. 5(j) shows σ/τ as a function of D for the driving forces $f_c = 0.2$ (orange triangles), 0.3 (green diamonds), 0.5 (red squares), and 1.2 (black circles). As can be clearly seen, in

Fig. 5(i) at constant D the change in σ/τ is more pronounced by increasing f_c as compared to its change at constant f_c when increasing D in Fig. 5(j).

D. Mean-square displacement

Next we consider the dynamics of the translocation process in more detail by monitoring different parts of the chain motion as a function of time. To this end the x component of the positions of the head monomer (the first monomer of the chain in terms of the chemical distance along the chain), the front monomer (leading edge of the chain in physical space, i.e., the monomer with the largest x coordinate), the center of mass of the whole chain (CM), and the center of mass for the *trans* side subchain (CM_{chl}), as well as the corresponding mean-square displacements (MSDs), are studied. Figure 6(a) shows the absolute value of the ensemble average of the x component of the position ($|\langle x \rangle|$) of the head monomer (black squares), front monomer (red circles), CM (green diamonds), and CM_{chl} (blue triangles) as a function of normalized time t/τ in log-log scale and for fixed $f_c = 1.2$ and $D = 6.0$. Figure 6(b) is the same as Fig. 6(a) but for fixed value of $f_c = 0.2$. Figures 6(c) and 6(d) are the same as Figs. 6(a) and 6(b), respectively, but for fixed $D = 2.0$. As $\langle x \rangle$ has negative values due to the local retracting movement of the monomers to the *cis* side at short times, this feature appears in Figs. 6(a)–6(d) as sharp valleys. These fluctuations clearly show that during the translocation process the monomers have back-and-forth movements at the entrance of the channel. The insets in Figs. 6(a)–6(d) present $\langle x \rangle$ as a function of t/τ on a linear-linear scale for the same

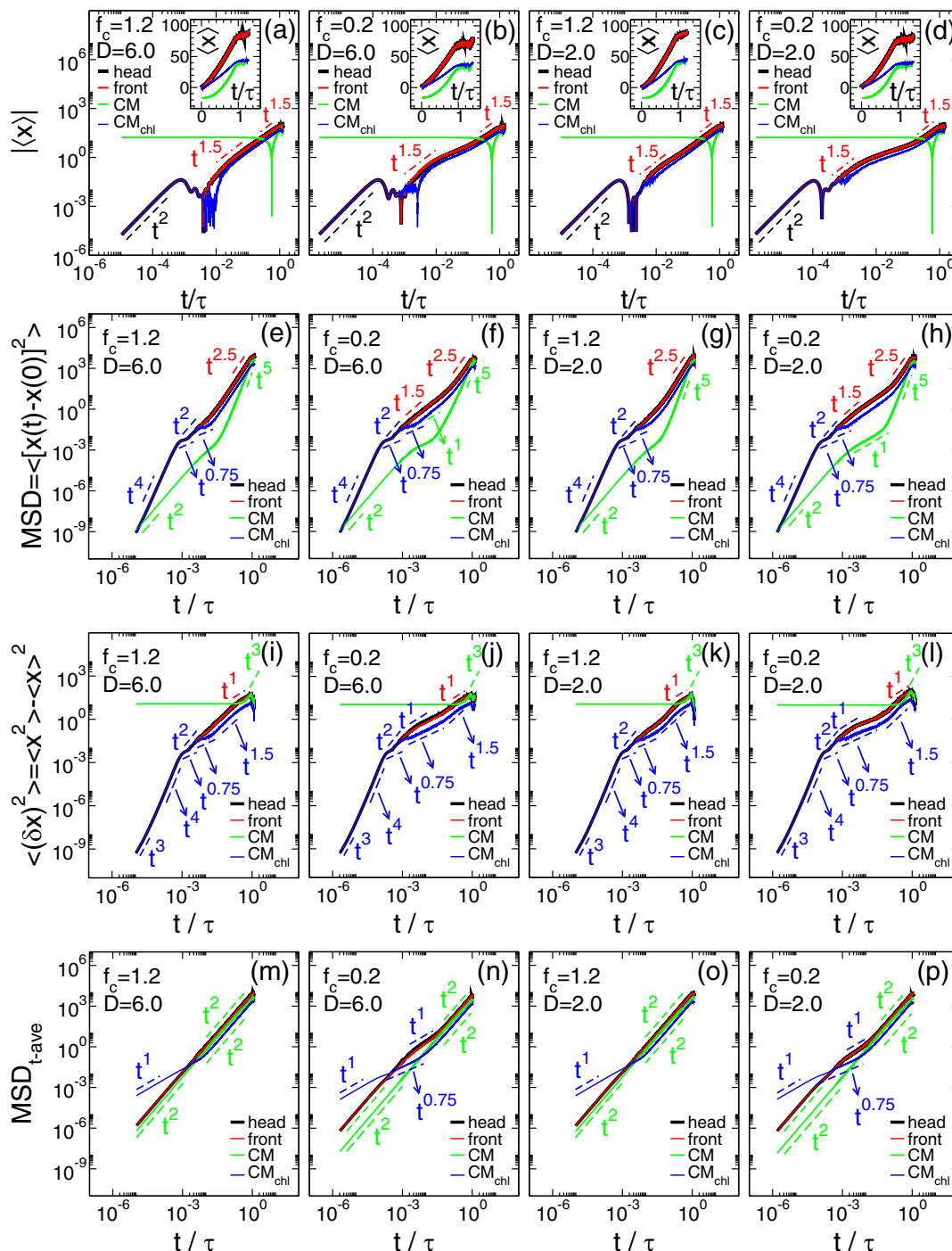


FIG. 6. (a) Absolute value of the horizontal ensemble average of the position $|\langle x \rangle|$ of the head (black squares), front (red circles), center of mass of the whole chain (CM) (green diamonds), and center of mass for the *trans* side subchain (CM_{chl}) (blue triangles) as a function of the normalized time t/τ in log-log scale for fixed values of the channel force $f_c = 1.2$ and channel diameter $D = 6.0$. The inset shows $\langle x \rangle$ as a function of t/τ in linear-linear scale for the same values of the parameters as in the main panel. (b) Same as (a) but for $f_c = 0.2$. (c) and (d) Same as (a) and (b), respectively, but for $D = 2.0$. (e) Ensemble-averaged MSD as a function of normalized time t/τ for the head (black line), front (red line), CM (green line), and CM_{chl} (blue line) as a function of t/τ for $f_c = 1.2$ and $D = 6.0$. (f) Same as (e) but for $f_c = 0.2$. (g) and (h) Same as (e) and (f), respectively, but for $D = 2.0$. The dashed lines and the slopes serve as a guide to the eye. (i)–(l) Variance $\langle (\delta x)^2 \rangle = \langle x^2 \rangle - \langle x \rangle^2$ as a function of t/τ . (m)–(p) Time-averaged MSD, MSD_{t-ave} , as a function of t/τ . All slopes in (a)–(p) are a guide to the eye.

values of parameters as in the corresponding main panels, for the head monomer (black squares) and front monomer (red circles) coincide with each other. Moreover, at short times the values of CM_{chl} (blue triangles) are the same as the values of the data for the head and front monomers; however, at long times its behavior is similar to that of CM.

In Fig. 6(e) the MSD $\langle [x(t) - x(0)]^2 \rangle$ is shown as a function of the normalized time t/τ with fixed values $f_c = 1.2$ and $D = 6.0$ for the head monomer (black solid line), front monomer (red solid line), CM (green solid line), and CM_{chl} (blue solid line). Figure 6(f) is the same as Fig. 6(e) but for fixed $f_c = 0.2$. Figures 6(g) and 6(h) are the same as Figs. 6(e) and 6(f), respectively, but for fixed $D = 2.0$. As seen in Figs. 6(e)–6(h), the behaviors of the MSD for the head, front, and CM_{chl} are similar to each other in almost all time regimes. At the very short times their local slope is 4, followed by 0.75 in the short time regime, then 2 and 1.5 at intermediate times, and finally 2.5 at long times. In contrast, the MSD for CM is different from the other MSDs in different time regimes. Indeed, the MSD slopes for CM are 2, 1, and 4 at very short, intermediate, and long time regimes, respectively.

Figure 6(i) shows the variance of the x component $\langle (\delta x)^2 \rangle = \langle x^2 \rangle - \langle x \rangle^2$ as a function of normalized time t/τ , with fixed $f_c = 1.2$ and $D = 6.0$, for the head monomer (black solid line), front monomer (red solid line), CM (green solid line), and CM_{chl} (blue solid line). Figure 6(j) is the same as Fig. 6(i) but for fixed $f_c = 0.2$. Figures 6(k) and 6(l) are the same as Figs. 6(i) and 6(j), respectively, but for fixed $D = 2.0$. The behavior of the variance for the head, front, and CM_{chl} in Figs. 6(e)–6(h) are again similar to each other. The slopes of the variance are 3, 4, 0.75, 2, and 1.5 at very short, short, intermediate, and long times, respectively. Conversely, for CM (green line) the slope is zero and becomes 3 at long times. All slopes in Figs. 6(a)–6(p) are a guide to the eye.

Finally, we consider the time-averaged MSD $MSD_{\text{t-ave}}$ computed as a running average over single trajectories [79,80]. Sampling positions as the time series $x(0), x(\Delta t), x(2\Delta t), x(3\Delta t), \dots, x[(n-1)\Delta t]$ with time step Δt , $MSD_{\text{t-ave}}$ at (lag) time $j\Delta t$ is defined as

$$MSD_{\text{t-ave}}(j\Delta t) = \frac{1}{n-j} \sum_{i=0}^{n-1-j} \{x[(i+j)\Delta t] - x(i\Delta t)\}^2, \quad (11)$$

where $j = 1, 2, 3, \dots, n-1$. In equilibrium systems (up to a factor of 2 occurring naturally due to the definition of $MSD_{\text{t-ave}}$ [81]) and systems with stationary increments $MSD_{\text{t-ave}}$ converges to the ensemble-averaged MSD $MSD = \langle [x(t) - x(0)]^2 \rangle$. Given small numbers of independent trajectories, the statistics of $MSD_{\text{t-ave}}$ for sufficiently long time series are often better than the ensemble-averaged MSD. For finite trajectories the time-averaged MSD fluctuates from one trajectory to the next, as often measured in terms of the ergodicity breaking parameter [82]. In weakly nonergodic systems [80,82,83] the time-averaged MSD may differ from the ensemble-averaged MSD even in the limit of long measurement times.

To check the above argument, in Fig. 6(m) $MSD_{\text{t-ave}}$ is shown as a function of normalized time t/τ with fixed $f_c = 1.2$ and $D = 6.0$ for the head monomer (black solid line), front

monomer (red solid line), CM (green solid line), and CM_{chl} (blue solid line). Figure 6(n) is the same as Fig. 6(m) but for the fixed value $f_c = 0.2$. Figures 6(o) and 6(p) are the same as Figs. 6(m) and 6(n), respectively, but for a fixed value of $D = 2.0$.

As Figs. 6(m)–6(p) clearly show, in the long time limit the data on all curves scale like t^2 . At very short times for CM_{chl} the time-averaged MSD scales as $MSD_{\text{t-ave}} \sim t^1$, while it scales as t^2 for the head, front, and CM. Moreover, in Figs. 6(n) and 6(p) in the weak force limit ($f_c = 0.2$) another intermediate scaling regime appears in which the time-averaged MSD for CM_{chl} scales as $t^{0.75}$. The time-averaged MSD analysis may thus provide additional information on the details of translocation processes; however, a more detailed study of the relation between ensemble- and time-averaged MSDs is beyond the scope of the present work.

E. Monomer density

Finally, we study the time evolution of the monomer density. It reveals the average spatial configuration of the polymer during the translocation process. In Fig. 7(a) the monomer density is shown for the maximum channel width $D_{\text{max}} = 6$ and channel driving force $f_c = 1.2$ at the times $t = 0, 0.2\tau, 0.4\tau, 0.6\tau$, and 0.8τ during the translocation process and for the final configuration. Averaging has been performed over 1000 independent trajectories. For the sake of better visibility, a blowup of the channel is added underneath the actual narrow channel. Inside the channel the size of the cells in the y and x directions is normalized by D_{max} and N_0 , respectively. At time zero the whole chain is on the *cis* side, and as the first bead is fixed at the entrance of the channel the polymer possesses an average pearlike shape. Over time more monomers traverse the channel entrance. At all moments of the translocation process the density of monomers around the corners of the channel entrance is higher than that along the channel axis due to the high driving force. At constant channel width $D_{\text{max}} = 6$ when the channel driving force decreases to $f_c = 0.2$ [Fig. 7(b)], the monomer density is more pronounced along the channel axis.

Figures 7(c) and 7(d) are the same as Figs. 7(a) and 7(b), respectively, but for channel width $D = 2$. A comparison of Figs. 7(c) and 7(d) reveals that by decreasing the channel width to $D = 2$, the narrowest one in the present study, as the monomers inside the channel do not have enough space in the y direction to perform significant spatial fluctuations, one finds them sharply around the channel axis, regardless of the value of the channel driving force. Moreover, it should be noted that the value of the monomer density in Figs. 7(c) and 7(d) is twice that in Figs. 7(a) and 7(b) (see the color bar).

V. SUMMARY AND CONCLUSIONS

In this work we have combined IFTP theory with extensive LD simulations to unravel the dynamics of polymer translocation into a long channel. The axial driving force f_c in this chain sucker scenario [36] acts on all monomers inside the channel, away from the pore (entry point of the channel), and the monomers inside the channel thus pull the other monomers on the *cis* side along. When the channel width D is wide

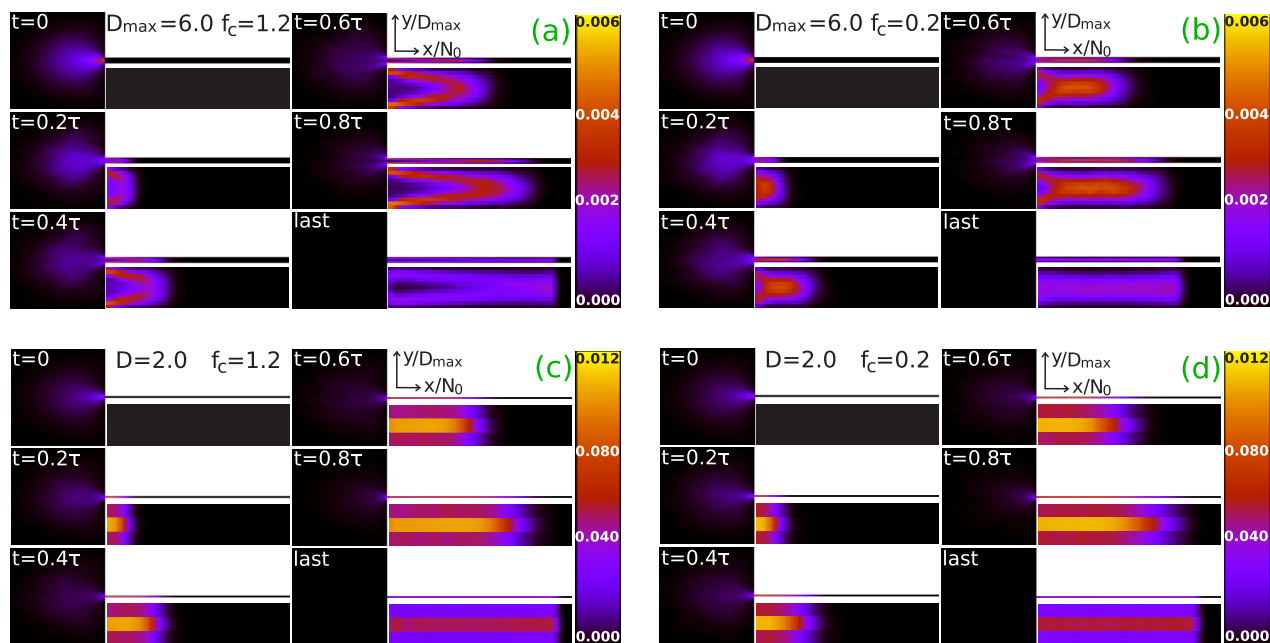


FIG. 7. (a) Two-dimensional monomer density of the chain on the *cis* as well as *trans* side at different times $t/\tau = 0, 0.2, 0.4, 0.6, \text{ and } 0.8$, as well as the final configurations of the chain, for fixed values of the channel width $D = 6.0$ and $f_c = 1.2$. Inside the channel the horizontal (parallel to the channel axis) and vertical distances are normalized by $N_0 = 100$ and $D_{\max} = 6.0$ (where D_{\max} is the maximum channel width), respectively. The monomer density of the *trans* side (channel) is also shown in a separate magnified panel below the actual much narrower channel for better visibility. (b) Same as (a) but for the weakest channel driving force in our LD simulations ($f_c = 0.2$). (c) and (d) Same as (a) and (b), respectively, but for the narrowest channel in the LD simulations ($D = 2.0$).

enough to allow the polymer to fluctuate in the channel, an entropic force due to the spatial fluctuations of the *trans* side subchain starts to play a role in the translocation dynamics when its magnitude becomes comparable to that of the driving force. Our analysis demonstrates how the *trans* side entropic force depends on the values of both D and f_c , as the spatial configuration of the *trans* side subchain is determined by both.

To further verify this, in Fig. 8(a) the horizontal size of the last configuration of the chain inside the channel R_{\parallel} is shown as a function of D for the channel driving force $f_c = 1.2$ (turquoise circles), 0.5 (orange squares), 0.3 (green diamonds), and 0.2 (pink triangles). The black solid curve is shown as a guide to the eye and depicts the scaling exponent for the equilibrium configuration of the chain inside a channel with width D . From blob theory the equilibrium axial chain-size exponent is $-1/3$ in the absence of any channel driving force $R_{\parallel} \propto D^{-1/3}$ [69]. As the driving force increases the axial chain-size exponent deviates from its equilibrium value of $-1/3$. Moreover, Fig. 8(b) shows that at constant D , the value of R_{\parallel} also depends on f_c . Therefore, Figs. 8(a) and 8(b) clearly confirm that R_{\parallel} depends on both f_c and D , and it is hard to separate the effect of their individual contributions to R_{\parallel} . In particular, the contributions of f_c and D to the entropic force are coupled to each other.

The only case in the present study wherein the *trans* side entropy does not play any significant role in the translocation dynamics is for the narrow channel width $D = 2$, and the corresponding LD result for the force exponent is $\beta = -1$ [orange dashed line in Fig. 4(a)], as predicted by IFTP theory wherein the contribution of the entropic force is not taken into account [see Eq. (10)]. As the value of D increases, the

trans side subchain possesses more spatial configurations and entropic force effects on the dynamics of translocation process

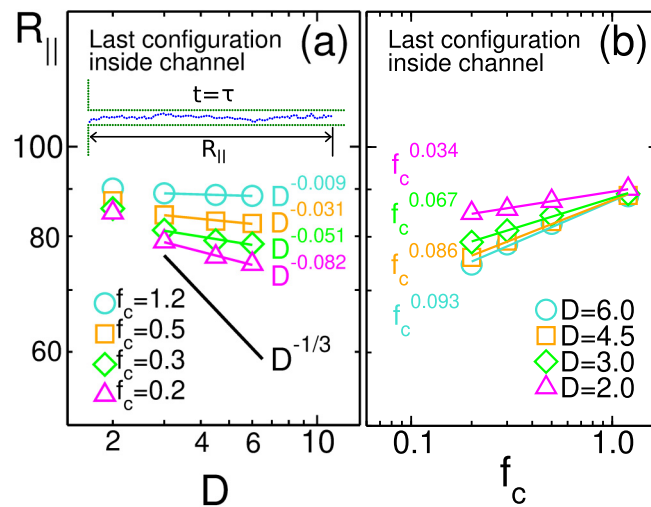


FIG. 8. (a) Horizontal size R_{\parallel} of the final chain configuration at the end of the translocation process, as a function of the channel width D , for the channel driving forces $f_c = 1.2$ (turquoise circles), 0.5 (orange squares), 0.3 (green diamonds), and 0.2 (pink triangles). As can be seen, all fitted slopes are far from the equilibrium behavior (for $f_c = 0$) with size exponent $-1/3$ (black solid curve as a guide to the eye). (b) Horizontal size R_{\parallel} as a function of f_c for channel widths $D = 6$ (turquoise circles), 4.5 (orange squares), 3 (green diamonds), and 2 (pink triangles), with the corresponding values of the exponents 0.034, 0.067, 0.86, and 0.093, respectively.

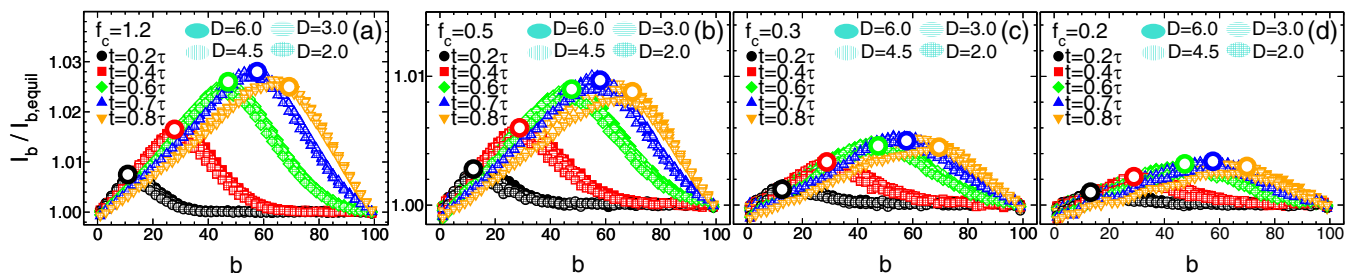


FIG. 9. (a) Normalized bond length $l_b/l_{b,eq}$ as a function of the bond index b for fixed channel driving force $f_c = 1.2$ and channel widths $D = 6.0$ (closed symbols), 4.5 (vertical hatching), 3.0 (horizontal hatching), and 2.0 (crosshatching), at times $t/\tau = 0.2$ (black circles), 0.4 (red squares), 0.6 (green diamonds), 0.7 (blue up-pointing triangles), and 0.8 (orange down-pointing triangles). (b)–(d) Same as (a) but for $f_c = 0.5, 0.3$, and 0.2 , respectively. Open circles approximately show the bond index inside the entrance of the channel at the corresponding times. Here $l_{b,eq} \approx 0.96$ is the equilibrium average value of the bond length.

are more pronounced, and consequently β deviates from -1 [see the inset of Fig. 4(a)].

Our study has unveiled a rich behavior of the observed translocation dynamics as a function of the system parameters of channel-driven translocation. Such scenarios are important for experimental systems such as long micro- or nanochannels that confine the DNA and apply flows along the channel [72–76].

ACKNOWLEDGMENTS

Computational resources from the Center for Scientific Computing Ltd. and from the Aalto University School of Science Science-IT project are gratefully acknowledged. T.A.N. was supported in part by the Academy of Finland through its PolyDyna (Grant No. 307806) and QFT Center of Excellence Program grants (Grant No. 312298). R.M. acknowledges the German Research Foundation (Grant No. ME 1535/12-1) and the Foundation for Polish Science (Humboldt Polish Honorary Research Scholarship) for support.

APPENDIX A: BOND LENGTH DISTRIBUTION

One of the quantities that show the dynamics of the translocation process at the monomer level is the bond length distribution. In Fig. 9 the normalized bond length $l_b/l_{b,eq}$ is shown as a function of the bond index b for constant channel driving force $f_c = 1.2$ and different channel widths $D =$

6.0 (closed symbols), 4.5 (vertical hatching), 3.0 (horizontal hatching), and 2.0 (crosshatching) at the times $t/\tau = 0.2$ (black circles), 0.4 (red squares), 0.6 (green diamonds), 0.7 (blue up-pointing triangles), and 0.8 (orange down-pointing triangles). Here $l_{b,eq} \approx 0.96$ is the average value of the bond length at equilibrium and τ is the average translocation time for the corresponding set of parameters. Figures 9(b)–9(d) are the same as Fig. 9(a) but for channel driving forces $f_c = 0.5, 0.3$, and 0.2 , respectively. As can be seen, at the beginning of the translocation process fewer bonds are affected by the tension force as compared to later times. At the TP time of about $t_{TP} = 0.7\tau$, all bonds in the polymer on average are stretched by the tension force. This is clearly shown by the blue curves in all panels of Fig. 9. As the channel driving force gets weaker [from Fig. 9(a) to Fig. 9(d)] the bonds are less stretched by the tension force. This is further confirmation for the existence of TP along the backbone of the chain. Each open circle approximately shows the bond index inside the entrance of the channel at the corresponding moment.

APPENDIX B: VELOCITY DISTRIBUTIONS FOR MONOMERS

We consider the monomer velocity distribution here. Its x component is obtained from averaging over 1000 uncorrelated trajectories for each set of parameters. In Fig. 10(a) the normalized x component of the monomer velocity v_x/f_c is shown as a function of the monomer index m for fixed

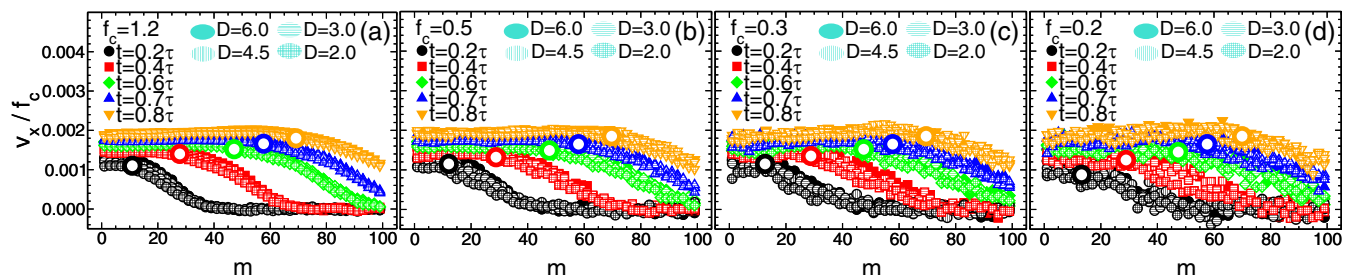


FIG. 10. (a) Normalized x component of the monomer velocity v_x/f_c as a function of the monomer index m , for fixed channel driving force $f_c = 1.2$ and channel widths $D = 6.0$ (closed symbols), 4.5 (vertical hatching), 3.0 (horizontal hatching), and 2.0 (crosshatching), during the translocation process at times $t/\tau = 0.2$ (black circles), 0.4 (red squares), 0.6 (green diamonds), 0.7 (blue up-pointing triangles), and 0.8 (orange down-pointing triangles). The open circles approximately specify the monomer index inside the entrance of the channel at the corresponding moments. (b)–(d) Same as (a) but for channel driving forces $f_c = 0.5, 0.3$, and 0.2 , respectively.

value of the channel driving force $f_c = 1.2$ and channel widths $D = 6.0$ (closed symbols), 4.5 (vertical hatching), 3.0 (horizontal hatching), and 2.0 (crosshatching) at different times $t/\tau = 0.2$ (black circles), 0.4 (red squares), 0.6 (green diamonds), 0.7 (blue up-pointing triangles), and 0.8 (orange down-pointing triangles). Figures 10(b)–10(d) are the same as Fig. 10(a) but for channel driving forces $f_c = 0.5, 0.3,$ and $0.2,$ respectively. To assess how the driving force affects the monomer velocity distribution, the normalized velocity has been plotted in all panels. As can be seen, the behavior of the curves at any given moment is similar for different values of the driving force. As the value of f_c decreases [from

Fig. 10(a) to Fig. 10(d)] the fluctuations in the curves increase, originating from two facts. The first one is that by decreasing the force the value of the normalized velocity increases (note that f_c is in the denominator of v_x/f_c) and this increases the fluctuations of the normalized velocity. The second reason is that by decreasing the driving force the tension force along the backbone of the chain becomes weaker, giving rise to more pronounced spatial fluctuations of the chain and consequently higher fluctuations of the monomer velocity. To have the same amount of monomer velocity fluctuations the average must be taken over more trajectories as the channel driving force decreases.

- [1] S. M. Bezrukov, I. Vodyanoy, and A. V. Parsegian, Counting polymers moving through a single ion channel, *Nature (London)* **370**, 279 (1994).
- [2] J. J. Kasianowicz, E. Brandin, D. Branton, and D. W. Deamer, Characterization of individual polynucleotide molecules using a membrane channel, *Proc. Natl. Acad. Sci. USA* **93**, 13770 (1996).
- [3] W. Sung and P. J. Park, Polymer Translocation through a Pore in a Membrane, *Phys. Rev. Lett.* **77**, 783 (1996).
- [4] A. Meller, L. Nivon, and D. Branton, Voltage-Driven DNA Translocations through a Nanopore, *Phys. Rev. Lett.* **86**, 3435 (2001).
- [5] A. F. Sauer-Budge, J. A. Nyamwanda, D. K. Lubensky, and D. Branton, Unzipping Kinetics of Double-Stranded DNA in a Nanopore, *Phys. Rev. Lett.* **90**, 238101 (2003).
- [6] A. J. Storm, J. H. Chen, X. S. Ling, H. W. Zandbergen, and C. Dekker, Fabrication of solid-state nanopores with single-nanometre precision, *Nat. Mater.* **2**, 537 (2003).
- [7] U. F. Keyser, B. N. Koeleman, S. van Dorp, D. Krapf, R. M. M. Smeets, S. G. Lemay, N. H. Dekker, and C. Dekker, Direct force measurements on DNA in a solid-state nanopore, *Nat. Phys.* **2**, 473 (2006).
- [8] E. H. Trepagnier, A. Radenovic, D. Sivak, P. Geissler, and J. Liphardt, Controlling DNA capture and propagation through artificial nanopores, *Nano Lett.* **7**, 2824 (2007).
- [9] S. van Dorp, U. F. Keyser, N. H. Dekker, C. Dekker, and S. G. Lemay, Origin of the electrophoretic force on DNA in solid-state nanopores, *Nat. Phys.* **5**, 347 (2009).
- [10] C. Raillon, P. Granjon, M. Graf, L. J. Steinbock, and A. Radenovic, Fast and automatic processing of multi-level events in nanopore translocation experiments, *Nanoscale* **4**, 4916 (2012).
- [11] F. Traversi, C. Raillon, S. M. Benameur, K. Liu, S. Khlybov, M. Tosun, D. Krasnozhan, A. Kis, and A. Radenovic, Detecting the translocation of DNA through a nanopore using graphene nanoribbons, *Nat. Nanotechnol.* **8**, 939 (2013).
- [12] R. D. Bulushev, S. Marion, and A. Radenovic, Relevance of the drag force during controlled translocation of a DNA-protein complex through a glass nanocapillary, *Nano Lett.* **15**, 7118 (2015).
- [13] M. Muthukumar, *Polymer Translocation* (Taylor and Francis, London, 2011).
- [14] V. V. Palyulin, T. Ala-Nissila, and R. Metzler, Polymer translocation: The first two decades and the recent diversification, *Soft Matter* **10**, 9016 (2014).
- [15] J. Sarabadani and T. Ala-Nissila, Theory of pore-driven and end-pulled polymer translocation dynamics through a nanopore: An overview, *J. Phys.: Condens. Matter* **30**, 274002 (2018).
- [16] A. Milchev, Single-polymer dynamics under constraints: Scaling theory and computer experiment, *J. Phys.: Condens. Matter* **23**, 103101 (2011).
- [17] M. Muthukumar, Polymer translocation through a hole, *J. Chem. Phys.* **111**, 10371 (1999).
- [18] J. Chuang, Y. Kantor, and M. Kardar, Anomalous dynamics of translocation, *Phys. Rev. E* **65**, 011802 (2001).
- [19] F. Tessier and G. W. Slater, Strategies for the separation of polyelectrolytes based on non-linear dynamics and entropic ratchets in a simple microfluidic device, *Appl. Phys. A* **75**, 285 (2002).
- [20] Y. Kantor and M. Kardar, Anomalous dynamics of forced translocation, *Phys. Rev. E* **69**, 021806 (2004).
- [21] T. Ambjörnsson and R. Metzler, Chaperone-assisted translocation, *Phys. Biol.* **1**, 77 (2004).
- [22] R. Zandi, D. Reguerra, J. Rudnick, and W. M. Gelbart, What drives the translocation of stiff chains?, *Proc. Natl. Acad. Sci. USA* **100**, 8649 (2003).
- [23] A. Y. Grosberg, S. Nechaev, M. Tamm, and O. Vasilyev, How Long Does It Take to Pull an Ideal Polymer into a Small Hole?, *Phys. Rev. Lett.* **96**, 228105 (2006).
- [24] K. Luo, T. Ala-Nissila, and S.-C. Ying, Polymer translocation through a nanopore: A two-dimensional Monte Carlo study, *J. Chem. Phys.* **124**, 034714 (2006).
- [25] T. Sakaue, Nonequilibrium dynamics of polymer translocation and straightening, *Phys. Rev. E* **76**, 021803 (2007).
- [26] G. Sigalov, J. Comer, G. Timp, and A. Aksimentiev, Detection of DNA sequences using an alternating electric field in a nanopore capacitor, *Nano Lett.* **8**, 56 (2008).
- [27] M. G. Gauthier and G. W. Slater, Nondriven polymer translocation through a nanopore: Computational evidence that the escape and relaxation processes are coupled, *Phys. Rev. E* **79**, 021802 (2009).
- [28] K. Luo, R. Metzler, T. Ala-Nissila, and S.-C. Ying, Polymer translocation out of confined environments, *Phys. Rev. E* **80**, 021907 (2009).
- [29] K. Luo, T. Ala-Nissila, S.-C. Ying, and R. Metzler, Driven polymer translocation through nanopores: Slow-vs.-fast dynamics, *Europhys. Lett.* **88**, 68006 (2009).
- [30] K. Luo and R. Metzler, Polymer translocation into laterally unbounded confined environments, *J. Chem. Phys.* **133**, 075101 (2010).

- [31] K. Luo and R. Metzler, Polymer translocation into a fluidic channel through a nanopore, *Phys. Rev. E* **82**, 021922 (2010).
- [32] T. Sakaue, Nonequilibrium dynamics of polymer translocation and straightening, *Phys. Rev. E* **81**, 041808 (2010).
- [33] H. W. de Haan and G. W. Slater, Mapping the variation of the translocation α scaling exponent with nanopore width, *Phys. Rev. E* **81**, 051802 (2010).
- [34] P. Rowghanian and A. Y. Grosberg, Force-driven polymer translocation through a nanopore: An old problem revisited, *J. Phys. Chem. B* **115**, 14127 (2011).
- [35] J. A. Cohen, A. Chaudhuri, and R. Golestanian, Active Polymer Translocation through Flickering Pores, *Phys. Rev. Lett.* **107**, 238102 (2011).
- [36] K. Luo and R. Metzler, The chain sucker: Translocation dynamics of a polymer chain into a long narrow channel driven by longitudinal flow, *J. Chem. Phys.* **134**, 135102 (2011).
- [37] T. Saito and T. Sakaue, Process time distribution of driven polymer transport, *Phys. Rev. E* **85**, 061803 (2012).
- [38] T. Ikonen, A. Bhattacharya, T. Ala-Nissila, and W. Sung, Unifying model of driven polymer translocation, *Phys. Rev. E* **85**, 051803 (2012).
- [39] T. Ikonen, A. Bhattacharya, T. Ala-Nissila, and W. Sung, Influence of non-universal effects on dynamical scaling in driven polymer translocation, *J. Chem. Phys.* **137**, 085101 (2012).
- [40] H. W. de Haan and G. W. Slater, Using an incremental mean first passage approach to explore the viscosity dependent dynamics of the unbiased translocation of a polymer through a nanopore, *J. Chem. Phys.* **136**, 204902 (2012).
- [41] N. Nikoofard, H. Khalilian, and H. Fazli, Directed translocation of a flexible polymer through a cone-shaped nano-channel, *J. Chem. Phys.* **139**, 074901 (2013).
- [42] J. Sarabadani, T. Ikonen, and T. Ala-Nissila, Iso-flux tension propagation theory of driven polymer translocation: The role of initial configurations, *J. Chem. Phys.* **141**, 214907 (2014).
- [43] A. Suma, A. Rosa, and C. Micheletti, Pore translocation of knotted polymer chains: How friction depends on knot complexity, *ASC Macro Lett.* **4**, 1420 (2015).
- [44] R. Adhikari and A. Bhattacharya, Translocation of a semiflexible polymer through a nanopore in the presence of attractive binding particles, *Phys. Rev. E* **92**, 032711 (2015).
- [45] J. Sarabadani, T. Ikonen, and T. Ala-Nissila, Theory of polymer translocation through a flickering nanopore under an alternating driving force, *J. Chem. Phys.* **143**, 074905 (2015).
- [46] T. Menais, S. Mossa, and A. Buhot, Polymer translocation through nano-pores in vibrating thin membranes, *Sci. Rep.* **6**, 38558 (2016).
- [47] J. Sarabadani, B. Ghosh, S. Chaudhury, and T. Ala-Nissila, Dynamics of end-pulled polymer translocation through a nanopore, *Europhys. Lett.* **120**, 38004 (2017).
- [48] A. Suma and C. Micheletti, Pore translocation of knotted DNA rings, *Proc. Natl. Acad. Sci. USA* **114**, E2991 (2017).
- [49] J. Sarabadani, T. Ikonen, H. Mökkönen, T. Ala-Nissila, S. Carson, and M. Wanunu, Driven translocation of a semi-flexible polymer through a nanopore, *Sci. Rep.* **7**, 7423 (2017).
- [50] T. Menais, Polymer translocation under a pulling force: Scaling arguments and threshold forces, *Phys. Rev. E* **97**, 022501 (2018).
- [51] S. Buyukdagli, J. Sarabadani, and T. Ala-Nissila, Dielectric trapping of biopolymers translocating through insulating membranes, *Polymers* **10**, 1242 (2018).
- [52] S. Buyukdagli, J. Sarabadani, and T. Ala-Nissila, Theoretical modeling of polymer translocation: From the electrohydrodynamics of short polymers to the fluctuating long polymers, *Polymers* **11**, 118 (2019).
- [53] A. Bhattacharya and S. Seth, Tug of war in a double-nanopore system, *Phys. Rev. E* **101**, 052407 (2020).
- [54] J. Sarabadani, S. Buyukdagli, and T. Ala-Nissila, Pulling a DNA molecule through a nanopore embedded in an anionic membrane: Tension propagation coupled to electrostatics, *J. Phys.: Condens. Matter* **32**, 385101 (2020).
- [55] B. Ghosh, J. Sarabadani, S. Chaudhury, and T. Ala-Nissila, Pulling a folded polymer through a nanopore, *J. Phys.: Condens. Matter* **33**, 015101 (2021).
- [56] H. Khalilian, J. Sarabadani, and T. Ala-Nissila, Polymer translocation through a nanopore assisted by an environment of active rods, *Phys. Rev. Research* **3**, 013080 (2021).
- [57] H. Ochman, J. G. Lawrence, and E. A. Groisman, Lateral gene transfer and the nature of bacterial innovation, *Nature (London)* **405**, 299 (2000).
- [58] S. Nakielny and G. Dreyfuss, Transport of proteins and RNAs in and out of the nucleus, *Cell* **99**, 677 (1999).
- [59] D. Branton *et al.*, The potential and challenges of nanopore sequencing, *Nat. Biotechnol.* **26**, 1146 (2008).
- [60] D. Deamer, M. Akeson, and D. Branton, Three decades of nanopore sequencing, *Nat. Biotechnol.* **34**, 518 (2016).
- [61] L. Messenger, J. R. Burns, J. Kim, D. Cecchin, J. Hindley, A. L. B. Pyne, J. Gaitzsch, G. Battaglia, and S. Howorka, Biomimetic hybrid nanocontainers with selective permeability, *Angew. Chem. Int. Ed.* **55**, 11106 (2016).
- [62] R. D. Bulushev, L. J. Steinbock, S. Khlybov, J. F. Steinbock, U. F. Keyser, and A. Radenovic, Measurement of the position-dependent electrophoretic force on DNA in a glass nanocapillary, *Nano Lett.* **14**, 6606 (2014).
- [63] R. D. Bulushev, S. Marion, E. Petrova, S. J. Davis, S. J. Maerkl, and A. Radenovic, Single molecule localization and discrimination of DNA-protein complexes by controlled translocation through nanocapillaries, *Nano Lett.* **16**, 7882 (2016).
- [64] F. Ritort, Single-molecule experiments in biological physics: Methods and applications, *J. Phys.: Condens. Matter* **18**, R531 (2006).
- [65] A. Fiasconaro, J. J. Mazo, and F. Falo, Active polymer translocation in the three-dimensional domain, *Phys. Rev. E* **91**, 022113 (2015).
- [66] R. I. Stefureac, A. Kachayev, and J. S. Lee, Modulation of the translocation of peptides through nanopores by the application of an AC electric field, *Chem. Commun.* **48**, 1928 (2012).
- [67] M. Bates, M. Burns, and A. Meller, Dynamics of DNA molecules in a membrane channel probed by active control techniques, *Biophys. J.* **84**, 2366 (2003).
- [68] G. J. Fleer, M. A. Cohen Stuart, J. M. H. M. Scheutjens, T. Cosgrove, and B. Vincent, *Polymers at Interfaces* (Chapman & Hall, London, 1998).
- [69] P.-G. de Gennes, *Scaling Concepts in Polymer Physics* (Cornell University Press, Ithaca, 1979).
- [70] K. Luo, T. Ala-Nissila, S.-C. Ying, and A. Bhattacharya, Influence of Polymer-Pore Interactions on Translocation, *Phys. Rev. Lett.* **99**, 148102 (2007).
- [71] H. Yong, Y. Wang, S. Yuan, B. Xu, and K. Luo, Driven polymer translocation through a cylindrical nanochannel: Interplay

- between the channel length and the chain length, *Soft Matter* **8**, 2769 (2012).
- [72] J. O. Tegenfeldt, C. Prinz, H. Cao, R. L. Huang, R. H. Austin, S. Y. Chou, E. C. Cox, and J. C. Sturm, Micro- and nanofluidics for DNA analysis, *Anal. Bioanal. Chem.* **378**, 1678 (2004).
- [73] J. O. Tegenfeldt, C. Prinz, H. Cao, S. Chou, W. W. Reisner, R. Riehn, Y. M. Wang, E. C. Cox, J. C. Sturm, P. Silberzan, and R. H. Austin, The dynamics of genomic-length DNA molecules in 100-nm channels, *Proc. Natl. Acad. Sci. USA* **101**, 10979 (2004).
- [74] Y. M. Wang, J. O. Tegenfeldt, W. Reisner, R. Riehn, X.-J. Guan, I. Golding, E. C. Cox, J. Sturm, and R. H. Austin, Single-molecule studies of repressor–DNA interactions show long-range interactions, *Proc. Natl. Acad. Sci. USA* **102**, 9796 (2005).
- [75] R. H. Liu and A. P. Lee, *Integrated Biochips for DNA Analysis* (Springer, Berlin, 2007), Chap. 12.
- [76] F. Persson and J. O. Tegenfeldt, DNA in nanochannels—Directly visualizing genomic information, *Chem. Soc. Rev.* **39**, 985 (2010).
- [77] G. S. Grest and K. Kremer, Molecular dynamics simulation for polymers in the presence of a heat bath, *Phys. Rev. A* **33**, 3628 (1986).
- [78] S. Plimpton, Fast parallel algorithms for short-range molecular dynamics, *J. Comput. Phys.* **117**, 1 (1995);
- [79] E. Barkai, Y. Garini, and R. Metzler, Strange kinetics of single molecules in living cells, *Phys. Today* **65(8)**, 29 (2012).
- [80] R. Metzler, J.-H. Jeon, A. G. Cherstvy, and E. Barkai, Anomalous diffusion models and their properties: Non-stationarity, non-ergodicity, and ageing at the centenary of single particle tracking, *Phys. Chem. Chem. Phys.* **16**, 24128 (2014).
- [81] J.-H. Jeon and R. Metzler, Inequivalence of time and ensemble averages in ergodic systems: Exponential versus power-law relaxation in confinement, *Phys. Rev. E* **85**, 021147 (2012).
- [82] Y. He, S. Burov, R. Metzler, and E. Barkai, Random Time-Scale Invariant Diffusion and Transport Coefficients, *Phys. Rev. Lett.* **101**, 058101 (2008).
- [83] J.-P. Bouchaud, Weak ergodicity breaking and aging in disordered systems, *J. Phys. (France) I* **2**, 1705 (1992).